Structure of Laminar Juncture Flows

Miguel R. Visbal*
Wright Research and Development Center, Wright-Patterson Air Force Base, Ohio 45433

A computational study of both steady and periodic laminar horseshoe vortex flows generated upstream of a cylinder/flat plate juncture is presented. The flowfields are simulated using the full three-dimensional unsteady Navier-Stokes equations and a time-accurate implicit algorithm. A new type of laminar horseshoe vortex topology is identified. For the case of a single primary vortex, this new topology is found to be independent of the computational grid and is also supported by recent experimental flow visualizations. The flat plate skin-friction portraits corresponding to the new and to the standard horseshoe vortex topologies are equivalent, pointing out the nonunique relation between the wall limiting streamline pattern and the three-dimensional flow above the plate. For the new topology, the foremost line of coalescense is an attachment rather than a separation line. This unusual feature illustrates the fact that convergence of skin-friction lines is a necessary but not sufficient condition for separation. As the Reynolds number increases, the flow topology evolves from a single to multiple primary horseshoe vortices, in agreement with experimental observations. At least two different types of triple horseshoe vortex systems are shown to be possible. Above a certain value of the Reynolds number, the juncture flow becomes unsteady and periodic at a frequency that increases with Reynolds number. The unsteady horseshoe vortex process upstream of the cylinder is found in qualitative agreement with experiment. Horseshoe vortices are periodically generated and convected toward the juncture. Vorticity intensification by vortex stretching, and the eruption of vorticity from the plate surface are observed.

Nomenclature

C_f	= flat plate skin-friction coefficient along symmetry line
D,h	= cylinder diameter and height, respectively
M_∞	= freestream Mach number
N, N'	= nodes and half-nodes, respectively
Re_D	= Reynolds number, $\rho_\infty U_\infty D/\mu_\infty$
S,S'	= saddle and half-saddle points, respectively
t^+	= nondimensional time, tU_∞/D
U_∞	= freestream velocity
x,y,z	= Cartesian coordinates
β_P	= separation parameter, $(\partial\omega_y/\partial x)/(\partial\omega_x/\partial y)$
δ_o	= incoming flat plate boundary-layer thickness
ξ, η, ς	= transformed coordinates
ω_x, ω_y, ω_z	= vorticity components in x, y, and z directions

Subscripts

A,S	= attachment and separation, respectively

I. Introduction

THE separated vortical flow generated at a wing-body juncture[1-3] constitutes an important example of interference flowfields and of three-dimensional separation. This flow configuration is not only rich in fundamental fluid mechanics phenomena, but is also present in numerous aerodynamic and hydrodynamic applications. For instance, juncture flows are of importance in external aerodynamics, turbomachinery, submarines, and wind-tunnel airfoil testing. The flowfield structure upstream of the junction is also related to the separated region formed upstream of a jet in crossflow.[4] The juncture formed by a circular cylinder placed on a flat plate along which a boundary layer is developing (Fig. 1) represents a model configuration to study the basic features of juncture flows. As the flow along the flat plate approaches the juncture, the large adverse pressure gradient induced by the cylinder produces boundary-layer separation as well as the formation of an array of horseshoe vortices. Depending on the flow conditions,[1-3] this array may be formed by one or more primary horseshoe vortices, accompanied by secondary counter-rotating vortical structures. These horseshoe vortices wrap around the cylinder and provide a mechanism for the diversion of low-energy boundary-layer fluid around the obstacle. In addition, these trailing regions of concentrated streamwise vorticity decay slowly[5] and interact with flow components downstream of the juncture.

Several experimental investigations of both steady and unsteady laminar juncture flows have been presented in the literature.[1,6-9] Examination of the available experimental evidence reveals that, as the Reynolds number increases, the topology of the three-dimensional separation evolves from a single primary horseshoe vortex to multiple vortices. Further increases in the Reynolds number result in unsteady laminar horseshoe vortex behavior that persists even when a splitter plate is placed behind the cylinder in order to suppress Karman vortex shedding. Although previous experimental work has provided a great deal of information about various aspects of laminar juncture flows, questions still remain unanswered regarding the precise flow topology and the unsteady horseshoe vortex phenomena, as well as their dependence on the various flow parameters (i.e., Reynolds number, cylinder aspect ratio, and incoming boundary-layer thickness). For instance, discrepancies in the horseshoe vortex system topology upstream of the juncture are apparent when comparing the inferred streamline patterns of Refs. 1 and 9-11. In addition, different types of unsteady horseshoe vortex phenomena are described by Baker,[1] Tobak and Peake,[6] and Thomas.[7] The discrepancies among the experiments, combined with the lack of detailed experimental measurements, indicate a need for further theoretical and experimental work on laminar juncture flows.

The present investigation provides a numerical study of both steady and unsteady laminar separated flows generated upstream of a cylinder/flat plate juncture. The main objectives of this work can be summarized as the following: 1) a description of the steady horseshoe vortex system topology upstream of the cylinder and its evolution with increasing Rey-

Presented as Paper 89-1873 at the AIAA 20th Fluid Dynamics, Plasma Dynamics, and Lasers Conference, Buffalo, NY, June 12-14, 1989; received Jan. 4, 1990; revision received Nov. 15, 1990; accepted for publication Nov. 23, 1990.

*Aerospace Engineer, Flight Dynamics Directorate. Member AIAA.

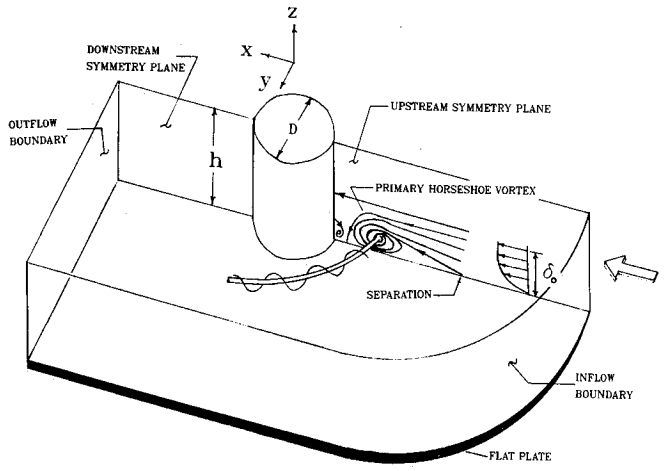

Fig. 1 Cylinder/plate juncture configuration.

nolds number, and 2) a preliminary study of the unsteady (periodic) horseshoe vortex phenomena.

In the present study, only one half of the cylinder/plate juncture flowfield is considered (Fig. 1). This symmetric configuration is chosen in order to completely isolate the cyclic horseshoe vortex process from Karman vortex shedding in the wake of the cylinder and to permit better numerical resolution of the pertinent flow features. The laminar juncture flows are simulated using the full three-dimensional unsteady Navier-Stokes equations and an implicit time-accurate approximate-factorization algorithm.[12] Although computations for steady laminar juncture flows have been conducted previously,[13,14] these studies have not simulated the topological change from a single to multiple primary horseshoe vortices associated with increasing Reynolds number. Finally, the simulation of the periodic laminar horseshoe vortex regime has not, to the author's knowledge, been previously presented in the literature.

II. Method of Solution

Governing Equations and Boundary Conditions

The governing equations are the full unsteady, three-dimensional compressible Navier-Stokes equations written in strong conservative form.[15] Closure of this system of equations is provided by the perfect gas law, Sutherland's viscosity formula, and the assumption of a constant Prandtl number ($Pr = 0.72$).

In reference to the computational domain shown in Fig. 1, the boundary conditions are prescribed as follows. On the cylinder and flat plate surfaces, no-slip, isothermal conditions are used in conjunction with a zero normal pressure gradient. At the inflow boundary, an incoming Blasius boundary-layer profile of thickness δ_o is prescribed. The velocity profile is approximated using Polhausen's formula,[16] with uniform flow outside the viscous region. On the outflow boundary, extrapolation of all flow variables is employed. Along the upper boundary, located at a nondimensional height h/D from the plate, symmetry conditions are applied. This situation corresponds to a cylinder of span $2h/D$ placed between end plates. The flow is assumed symmetric with respect to $y = 0$, and, therefore, symmetry conditions are invoked on the corresponding boundaries, as shown in Fig. 1. Finally, replacement of the symmetry condition in the wake by a splitter-plate boundary condition produced no changes in the horseshoe vortex structure upstream of the cylinder.

Numerical Procedure

Computational grids for the cylinder/flat plate juncture are obtained by stacking, according to a suitable z-distribution, identical two-dimensional plane grids. The two-dimensional grid about the cylinder is of the C-type and is generated using a hyperbolic mesh generation technique.[17] Figure 2 shows the grid structure in the vicinity of the juncture. Grid clustering is provided near the upstream symmetry plane and next to the cylinder and flat plate surfaces, respectively. The base grid employed in the majority of the computations has dimensions ($95 \times 197 \times 41$) in ξ, η, and ς, respectively. The inflow and outflow boundaries (Fig. 1) are located approximately 20 and 15 diameters away from the cylinder. The minimum grid spacing in the ξ direction is $0.0025D$ and $0.0005D$ normal to the solid surfaces. Typically, more than 25 points are placed within the incoming laminar boundary layer.

The governing equations are numerically solved employing the implicit approximate-factorization Beam-Warming algorithm.[12] The scheme is formulated using Euler implicit time-differencing and second-order finite-difference approximations for all spatial derivatives. Constant coefficient fourth-order explicit and second-order implicit damping terms are added for numerical stability. A fully vectorized, time-accurate, three-dimensional Navier-Stokes solver has been developed using the aforementioned numerical method. The code has been successfully validated for a variety of both steady and unsteady laminar test flow cases, including Couette flow formation, flat plate boundary layer, vortex shedding behind a circular cylinder, Taylor-vortex flow,[18] and delta-wing flows.[19,20]

III. Results and Discussion

Unless otherwise noted, computational results were obtained on the base grid ($95 \times 197 \times 41$) discussed in Sec. II with the flow parameters $M_\infty = 0.2$, $\delta_o/D = 0.1$, and $h/D = 2.0$. Various Reynolds numbers were considered, ranging from $Re_D = 5 \times 10^2$ to 5.4×10^3. For the case of steady juncture flows, convergence was assured by monitoring the evolution of the flat plate skin-friction coefficient along the line of symmetry upstream of the cylinder. The sensitivity of the computed flowfield to grid resolution and numerical damping was investigated[18] for $Re_D = 1.5 \times 10^3$. Variations in the skin-friction coefficient beneath the horseshoe vortex system due to grid spacing and damping coefficient were not significant. Most important, the flow topology in the forward plane of symmetry was found to be independent of the previously mentioned numerical parameters. Further evidence of grid independence for the computed flow topology is presented below for the case of $Re_D = 5 \times 10^2$.

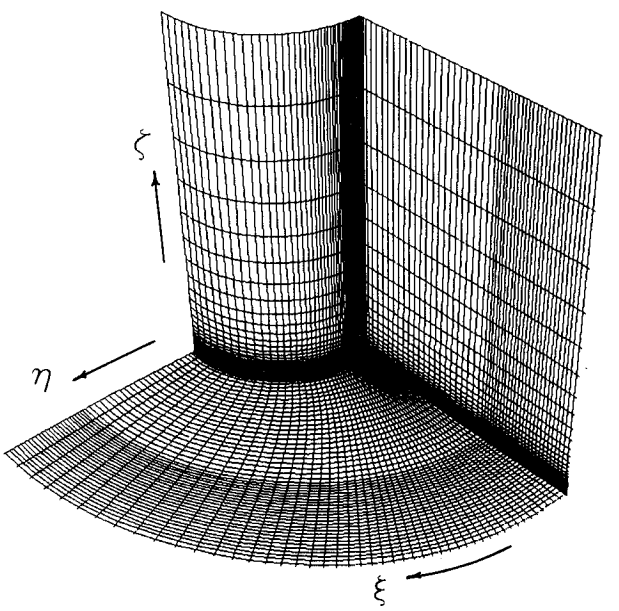

Fig. 2 Computational grid structure.

Steady Single Primary Horseshoe Vortex System

The computed flowfield structure on the plane of symmetry for $Re_D = 5 \times 10^2$ is shown in Fig. 3. At this Reynolds number, a primary horseshoe vortex forms upstream of the cylinder and represents the simplest laminar horseshoe vortex topology computed in the present study. The limiting streamline pattern on the flat plate, shown in Fig. 4, is characterized by a line of coalescense (with its associated saddle point S) and by a line of divergence (with its associated node N). The skin-friction coefficient along the symmetry line upstream of the juncture (Fig. 5) displays two points of zero C_f, which correspond to the saddle and node of Fig. 4. Although the surface streamline pattern is of the type usually described in the literature,[6,10] the streamline pattern in the symmetry plane represents a new topology not previously recognized to exist in laminar juncture flows.

In order to clarify the differences between the computed new topology and the standard topology in the symmetry plane, sketches of both topologies are shown in Fig. 6. The streamline patterns of Figs. 6a and 6b display similarities, including the existence of reversed flow downstream of point P, as well as the spiraling pattern of the horseshoe vortex. However, a fundamental difference between the two topologies arises due to the structure of the flow in the vicinity of point P. In the standard case (Fig. 6a), P is a half-saddle point of separation (denoted as S_s'), whereas in the computed topology (Fig. 6b), P is a half-node of attachment (denoted as N_A'). These two distinct flow topologies near P were predicted analytically by Perry and Fairlie[11] in 1974 as possible cases of symmetric three-dimensional laminar separation. The term separation is, however, ambiguous when referring to the topology of Fig. 6b since, although there is reversed flow downstream of P, P is actually a node of attachment. Despite the analytic work of Ref. 11, the type of separation of Fig. 6b has been ignored in the literature of laminar juncture flows, including by Perry and Fairlie who conjectured point P to be a separation point when interpreting experimental smoke visualizations of a cylinder/plate juncture. The type of flow topology near P is actually determined[11] through examination of the value of the separation parameter $\beta_P = (\partial\omega_y/\partial x)/(\partial\omega_x/\partial y)$, where ω_x and ω_y denote the vorticity components in the x and y directions, respectively. For $\beta_P > 1$, P is a separation point (Fig. 6a), whereas for $\beta_P < 1$, P is a point of attachment. In the present computations with $Re_D = 5 \times 10^2$, β_P was found to be less than unity, consistent with the flow topology (near P) of Fig. 6b.

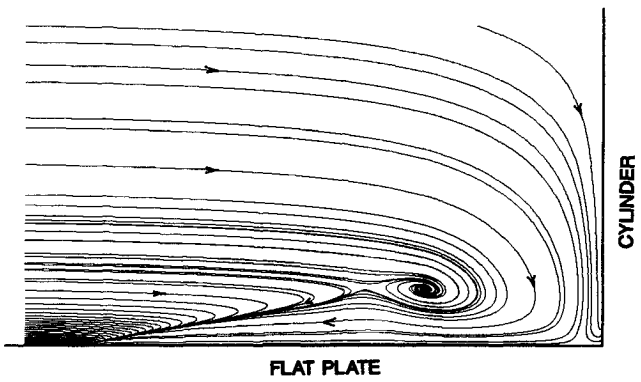

Fig. 3 Streamline pattern on symmetry plane, $Re_D = 5 \times 10^2$.

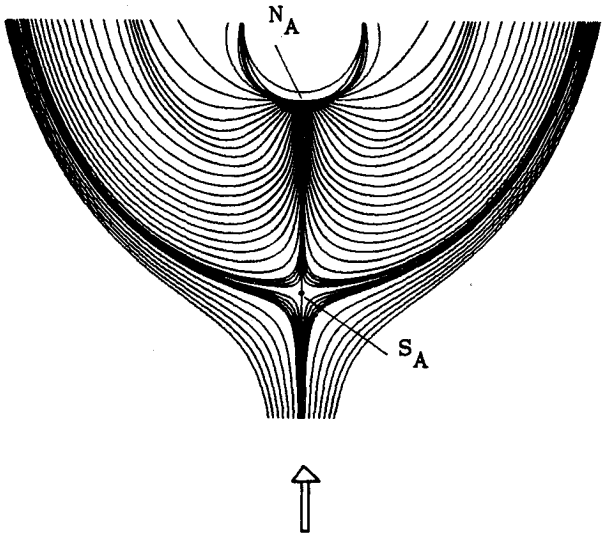

Fig. 4 Limiting streamline pattern on flat plate, $Re_D = 5 \times 10^2$.

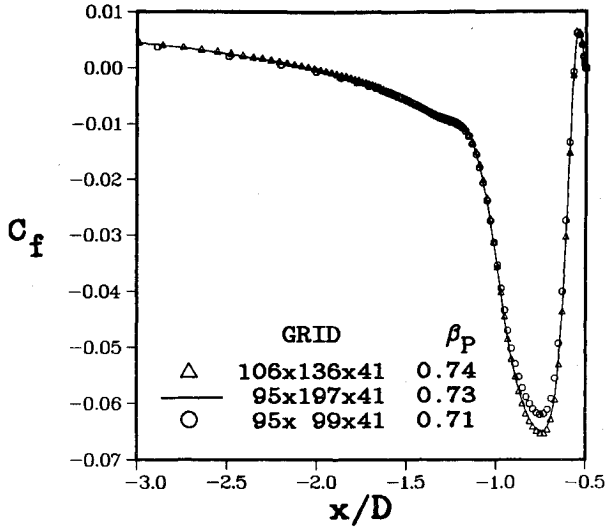

Fig. 5 Flat plate skin-friction coefficient upstream of the cylinder for $Re_D = 5 \times 10^2$: The grid spacing in the ξ and η directions are: △, 0.01D, 0.05D; —, 0.04D, 0.1D; ○, 0.04D, 0.2D.

In order to further support the present results, the juncture flow for $Re_D = 5 \times 10^2$ was computed using three different grid systems, thereby varying the mesh spacing near point P by a factor of 4 in both the radial and azimuthal directions. As shown in Fig. 5, the skin-friction coefficient and the separation location were found to be nearly grid independent. Most important, the separation parameter β_P, which controls the flow topology, remained nearly constant (between 0.71–0.74). Furthermore, an experimental confirmation of the computed new topology has been given by Kawahashi and Hosoi[21] subsequent to the present computational study. Figure 7, taken from Ref. 21, shows a laser specklegram of the flowfield in the symmetry plane upstream of a cylinder/flat plate juncture. The experimentally observed horseshoe vortex structure displays the new topology predicted in the computations (Fig. 3).

Implications of the New Topology on the Interpretation of Experimental Oil-Flow Patterns

Although the symmetry plane streamline patterns of Figs. 6a and 6b are fundamentally different, their corresponding skin-friction portraits on the flat plate are equivalent (Figs. 4 and 6c), a point that illustrates the nonunique relation between the surface flow pattern and the three-dimensional flow above the plate.[22] Experimental oil-flow visualizations cannot, therefore, distinguish between the two types of horseshoe vortex topologies unless the parameter β_P or the symmetry-plane flow is also obtained. In both topologies, the surface

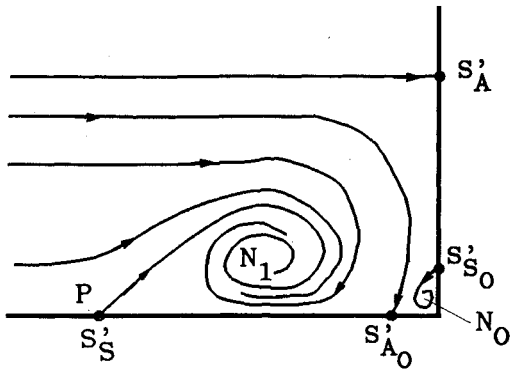

a) Standard topology on symmetry plane

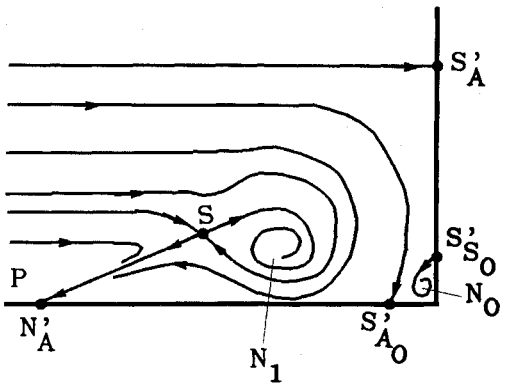

b) Computed new topology on symmetry plane

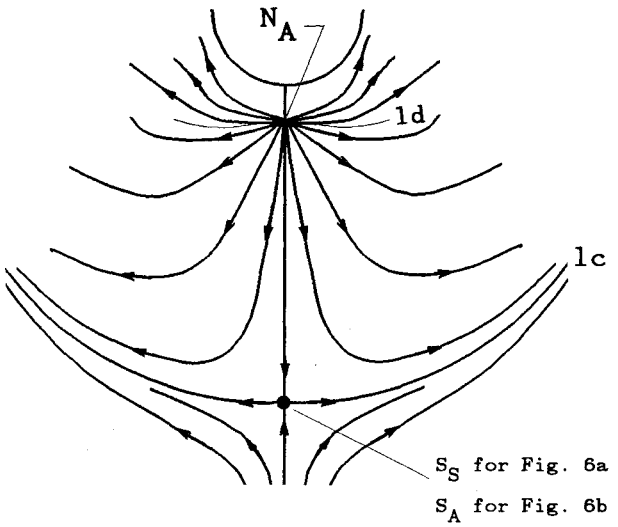

c) Corresponding footprint on flat plate for both a and b

Fig. 6 Topology of single primary horseshoe vortex system.

streamline pattern (Fig. 6c) is characterized by a line of coalescense (1c) and a line of divergence (1d). For the standard topology, the line of convergence in the wall streamlines is a separation line (saddle point of separation), whereas for the new topology, this line of convergence is, indeed, an attachment line (saddle point of attachment).[23] In the interpretation of experimental oil-flow visualizations, lines of coalescense are usually equated with separation. The computed and experimentally confirmed new topology clearly illustrates the fact that convergence of oil-streak lines is a necessary but not sufficient condition for separation, a point that has been the subject of debate.[23,24] The computed new laminar horseshoe vortex topology represents, to the author's knowledge, the first actual vortical flow case in which a line of oil accumulation represents an attachment line. Although Perry and Fairlie[11] identified analytically the two different types of symmetric, three-dimensional laminar separation, they did not elaborate on the implications for the interpretation of experimental oil-flow visualizations.

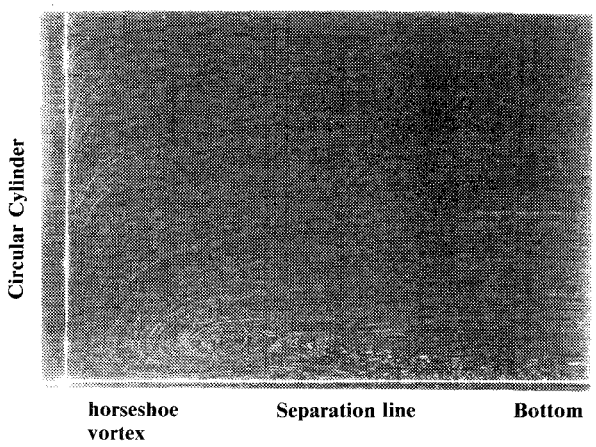

Fig. 7 Experimental flow visualization on upstream symmetry plane, taken from Ref. 21.

Steady Multiple Horseshoe Vortex Systems

Steady laminar juncture flows were also computed for $Re_D = 1.5 \times 10^3$ and 2.6×10^3, with $\delta_o/D = 0.1$. At $Re_D = 1.5 \times 10^3$, two primary horseshoe vortices formed upstream of the cylinder. This flow topology can be found in Ref. 18. For $Re_D = 2.6 \times 10^3$, three primary horseshoe vortices appeared, as shown in Fig. 8a. Two of the secondary vortical structures can also be observed in Fig. 8b. This case represents the most complex steady horseshoe vortex array computed in the present study. The surface streamline pattern on the plate, shown in Fig. 9, displays three lines of convergence (denoted as lc_1, lc_2, lc_3) and three lines of divergence (ld_1, ld_2, ld_3) consistent with the triple horseshoe vortex system in the symmetry plane (Fig. 8). The divergence lines are lines of attachment. The coalescense lines lc_1 and lc_2 are lines of separation, whereas the outermost convergence line lc_3 is a line of attachment, as previously discussed for the single primary horseshoe vortex system. Here again, the separation parameter β_P was found to be < 1 ($\beta_P = 0.93$) consistent with the observed flow topology of Fig. 8.

A schematic of the computed triple horseshoe vortex array topology is given in Fig. 10a along with the standard jet-maze topology described in the literature[9,10] (Fig. 10b). A fundamental difference between the two topologies arises again due to the flow structure near the point P, which is controlled by the parameter β_P ($\beta_P < 1$ in Fig. 10a, $\beta_P > 1$ in Fig. 10b). Important differences also exist regarding the way in which each of the primary vortices is fed by the incoming flow. For the computed topology of Fig. 10a, and proceeding toward the plate, vortex 1 is fed first by region ab, then vortex 2 by region cd, and finally vortex 3 by region ef. For the classical topology of Fig. 10b, vortex 3 is fed first by region ab, then vortex 2 by region bc, and later vortex 1 by region cd. Subsequently, vortices 2 and 3 are fed once again by regions de and ef, respectively.

In order to demonstrate that both topologies of Fig. 10 are possible, a computation was performed for a much thinner incoming boundary layer with $Re_D = 5 \times 10^3$ and the flat plate leading edge located at $x/D = -2.0$. This case resulted in a value of β_P of 1.2; thus, the classical flow topology is expected to exist. The computed symmetry plane streamline pattern is shown in Fig. 11. This topology is indeed of the standard type shown in Fig. 10b, except for a missing secondary structure not resolvable by the grid employed.

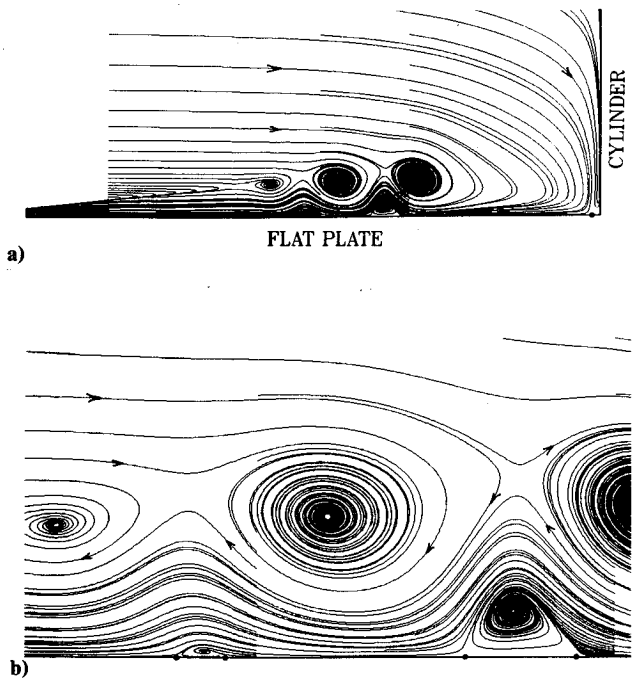

Fig. 8 Streamline pattern on symmetry plane, $Re_D = 2.6 \times 10^3$.

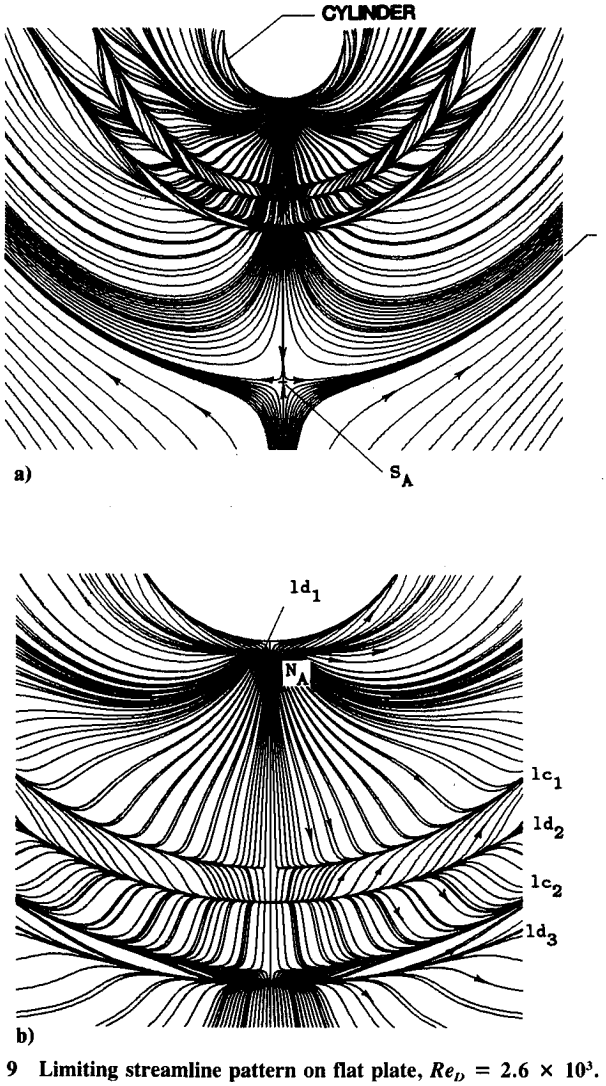

Fig. 9 Limiting streamline pattern on flat plate, $Re_D = 2.6 \times 10^3$.

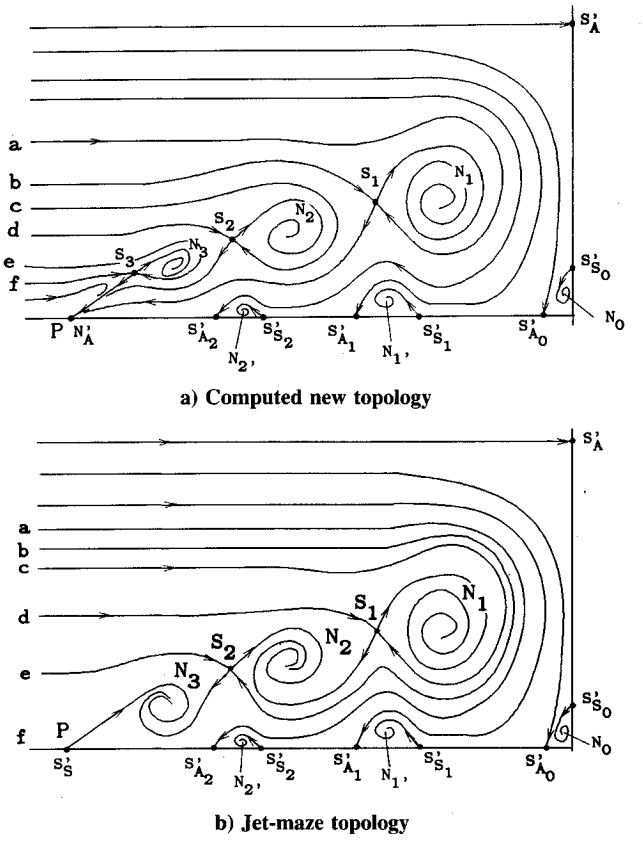

Fig. 10 Topology of triple primary horseshoe vortex system.

The present results indicate that the two different horseshoe vortex systems of Figs. 10 are possible. The actual type of topology that will prevail in a given case will be determined by the parameter β_P. The dependence of this parameter on Re_D, δ_o/D and h/D remains the subject of future study. In addition, the new multiple vortex topology of Fig. 10a is in need of experimental confirmation, as it was done for the single horseshoe vortex case.[21] To this effect, flow visualization techniques of greater resolution than simple smoke visualizations might be required.

Finally, the triple horseshoe vortex array topology presented by Baker[1] is different from the two types previously described. However, as noted by Baker, the topology in Ref. 1 is partially conjectured since it was not clear which of vortices 2 or 3 was fed first as the smoke probe was brought closer to the plate in the experiment. All that can be said with certainty about the topology of Ref. 1 is that it was not of the standard type (Fig. 10b) since vortex 1 was definitely fed before vortices 2 and 3 in the experiment. It is interesting to note that, if Baker had assumed vortex 2 to be fed before vortex 3, the order of feeding of the vortices would have corresponded to the new topology of Fig. 10a. The multiple vortex topology conjectured by Baker[1] also displays an unusual saddle-to-saddle-point connection. The symmetry-plane streamline patterns of Figs. 10, as well as that of Baker,[1] all satisfy the following topological constraint[24,25]

$$\Sigma_N + \tfrac{1}{2}\Sigma_{N'} - [\Sigma_S + \tfrac{1}{2}\Sigma_{S'}] = 0$$

where Σ denotes the number of corresponding singular points. In addition, the corresponding skin-friction portraits on the flat plate are all equivalent, emphasizing the limitations of oil-flow visualizations.

Unsteady Horseshoe Vortex Systems

The computed juncture flow became unsteady and cyclic for $Re_D = 4 \times 10^3$ and 5.4×10^3 (with $\delta_o/D = 0.1$). In order to rule out the possibility of nonphysical, numerically induced

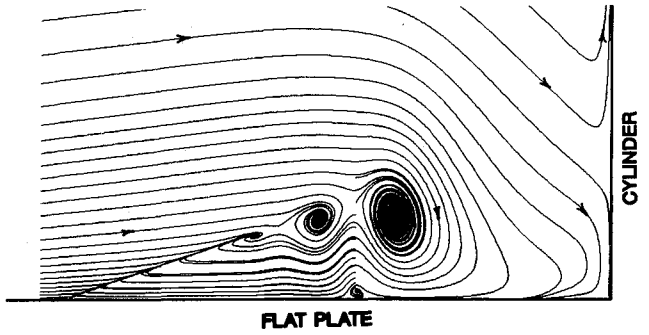

Fig. 11 Computed streamline pattern on symmetry plane, Re_D = 5 × 10³ and flat plate leading edge at $x/D = -2.0$.

unsteadiness, various computational parameters were varied, including time step, damping coefficient, and grid spacing in the radial direction. In all cases, the unsteady behavior persisted, qualitatively unaltered. This indicates that the numerical procedure is capable of reproducing the experimentally observed[1,6-8] natural unsteadiness encountered, above certain Reynolds numbers, in laminar juncture flows. The computed unsteady horseshoe vortex phenomena was found to be qualitatively the same for both $Re_D = 4 \times 10^3$ and 5.4×10^3. Furthermore, in agreement with the experiments of Ref. 7, the frequency of the unsteady process increased with Reynolds number. In this section, the cyclic horseshoe vortex flow is presented only for $Re_D = 5.4 \times 10^3$. Approximately eight cycles were computed for this case in order to confirm the persistence of the unsteady behavior. Figure 12 shows the time history (for the last four cycles) of the skin-friction coefficient at a point along the symmetry line upstream of the juncture ($x/D = -1.0$). The cyclic, quasiperiodic behavior is apparent. The Strouhal number $St = fD/U_\infty$ based on the last cycle was 0.21, which is in close agreement with the experimental value of 0.20 obtained by Thomas[7] for the same Reynolds number, albeit for different values of h/D and δ_o/D.

In what follows, the unsteady horseshoe vortex phenomenon is described by examination of the flowfield upstream of the cylinder. In the experiments,[7] an unusual horseshoe vortex pinchoff mechanism appears to take place behind the cylinder. However, marginal numerical grid resolution in that region precludes a conclusive description of such process at present. In addition to the horseshoe vortices, other unsteady

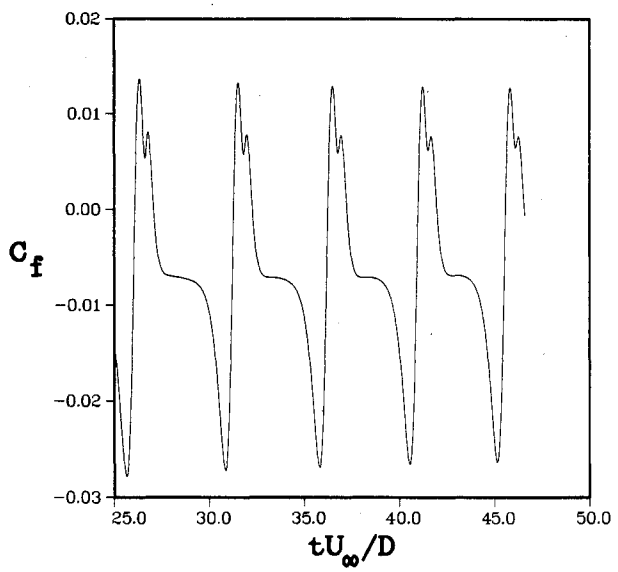

Fig. 12 Time history of flat plate skin-friction coefficient beneath unsteady horseshoe vortex system, $Re_D = 5.4 \times 10^3$, $x/D = -1.0$.

vortical structures (not shown) exist in the wake of the cylinder with spiraling cores that lift off the flat plate surface. The complex unsteady vortical flow behind the juncture remains the subject of future investigation. The present results for the unsteady flow upstream of the juncture are, nonetheless, expected to be valid based on two main reasons. First, the computed unsteady horseshoe vortex process and its frequency are in agreement with the experiments of Thomas.[7] Second, according to Baker,[1] modifications in the wake of the cylinder did not affect the experimentally observed unsteadiness upstream of the juncture.

Figure 13 shows the instantaneous streamlines on the symmetry plane for one cycle of the unsteady process. At a given instant, three or four primary vortices (denoted as 1,2,3,4) can be observed. In addition, some of the secondary vortices are discernable. The topology upstream of vortex 1 (Fig. 13d) is of the new type previously described for steady horseshoe vortex systems (Fig. 10a). That is to say, the foremost singular point is a half-node of attachment N_A, and a saddle point exists between this node and vortex 1. The separation parameter β_P, although variable in time, remained < 1 in accordance with the observed flow topology. Figure 14 shows schematically the evolution of the topology for the secondary flow between vortices 1 and 2, corresponding to Figs. 13a–f. As the strength of vortex 2 increases, the node in Fig. 14a is lifted off the surface and eventually disappears (Fig. 14f). It is interesting to note that during this process the corresponding skin-friction portrait remains qualitatively unaltered. The evolution of the streamline topology for the region between vortices 2 and 3 (Figs. 13a–e) is precisely the reverse sequence of that shown in Fig. 14. The instantaneous streamline pattern of Fig. 14e is similar to one of the steady two-dimensional topologies constructed analytically by Perry and Chong.[26]

Although instantaneous streamlines provide information about some of the features of the unsteady horseshoe vortex system, interpretation of the flow physics based solely on streamlines can be misleading since their complex pattern depends on the relative position and strength of neighboring vortical structures. In order to assess the effects of vortex stretching and viscous dissipation on the horseshoe vortices, the vorticity field must be examined. Figure 15 shows the evolution of the vorticity contours in the vicinity of vortex 3. In addition, the time history of the maximum vorticity value at the core of the horseshoe vortex (Fig. 16a) and its trajectory (Fig. 16b) are given.

From the instantaneous streamlines and the vorticity field on the symmetry plane, the following features of the cyclic horseshoe vortex phenomena can be observed.

1) New horseshoe vortices are periodically generated downstream of the node of attachment (see vortex 1, Figs. 13a–d). Unlike the standard topology of Fig. 10b where the horseshoe vortex is connected to the plate by a surface of separation, in the present case, the vortex is essentially free to move without having to be shed from the surface. The horseshoe vortex is convected toward the cylinder (see vortices 1 and 2, Fig. 13) in an initially horizontal path, as shown in Fig. 16b.

2) As vortex 3 in Fig. 13 illustrates, the horseshoe vortex moves very close to the cylinder. During this stage, the maximum vorticity value drastically increases due to vortex stretching (Fig. 16a) and reaches its greatest intensity when the vortex is in closest proximity to the cylinder. As expected, the vortex cross section decreases in size and the vorticity gradients are also enhanced (Fig. 15). As the vorticity intensifies, a very interesting vortex/surface interaction takes place that was not previously apparent from the instantaneous streamline patterns.[7] Vorticity of opposite sign to that of the horseshoe vortex erupts from the flat plate boundary layer (Fig. 15a). This vorticity orbits in a counterclockwise sense around the horseshoe vortex (Fig. 15b) due to the velocity field induced by vortex 3 and eventually wraps all the way around the vortex (Fig. 15c). Although only the symmetry

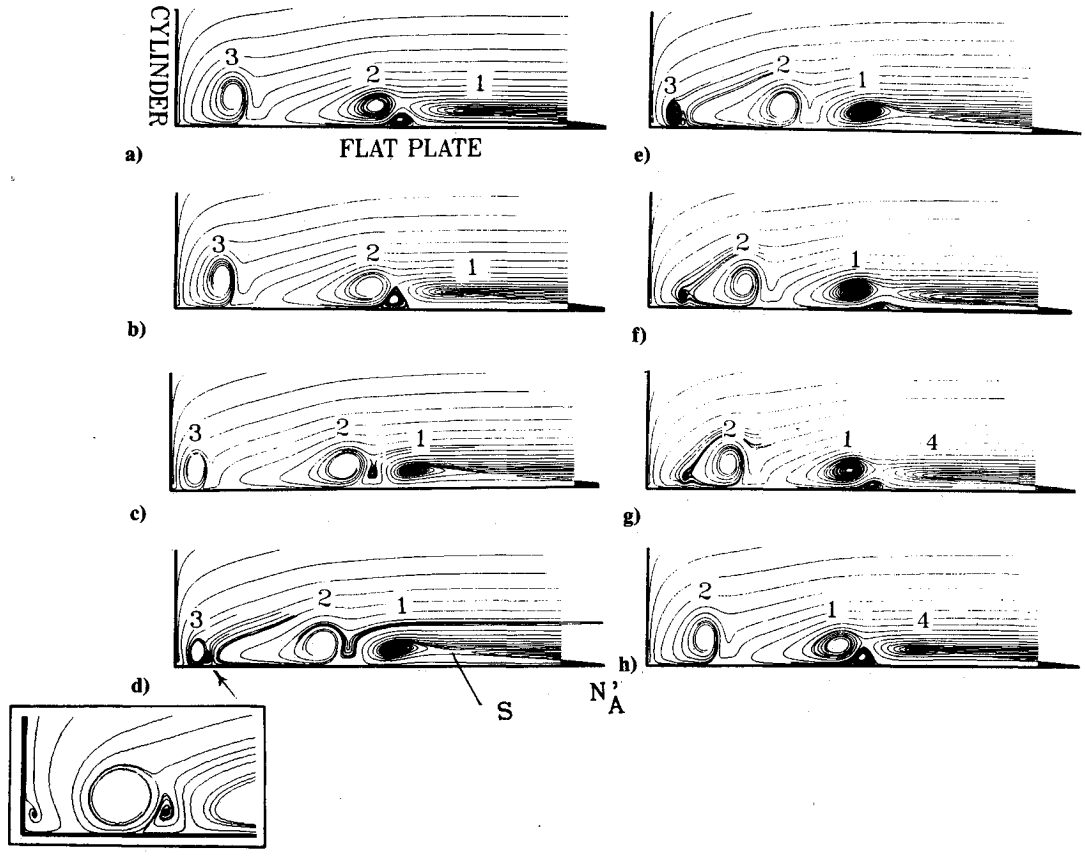

Fig. 13 Evolution of streamline pattern on symmetry plane for one cycle of motion, $Re_D = 5.4 \times 10^3$

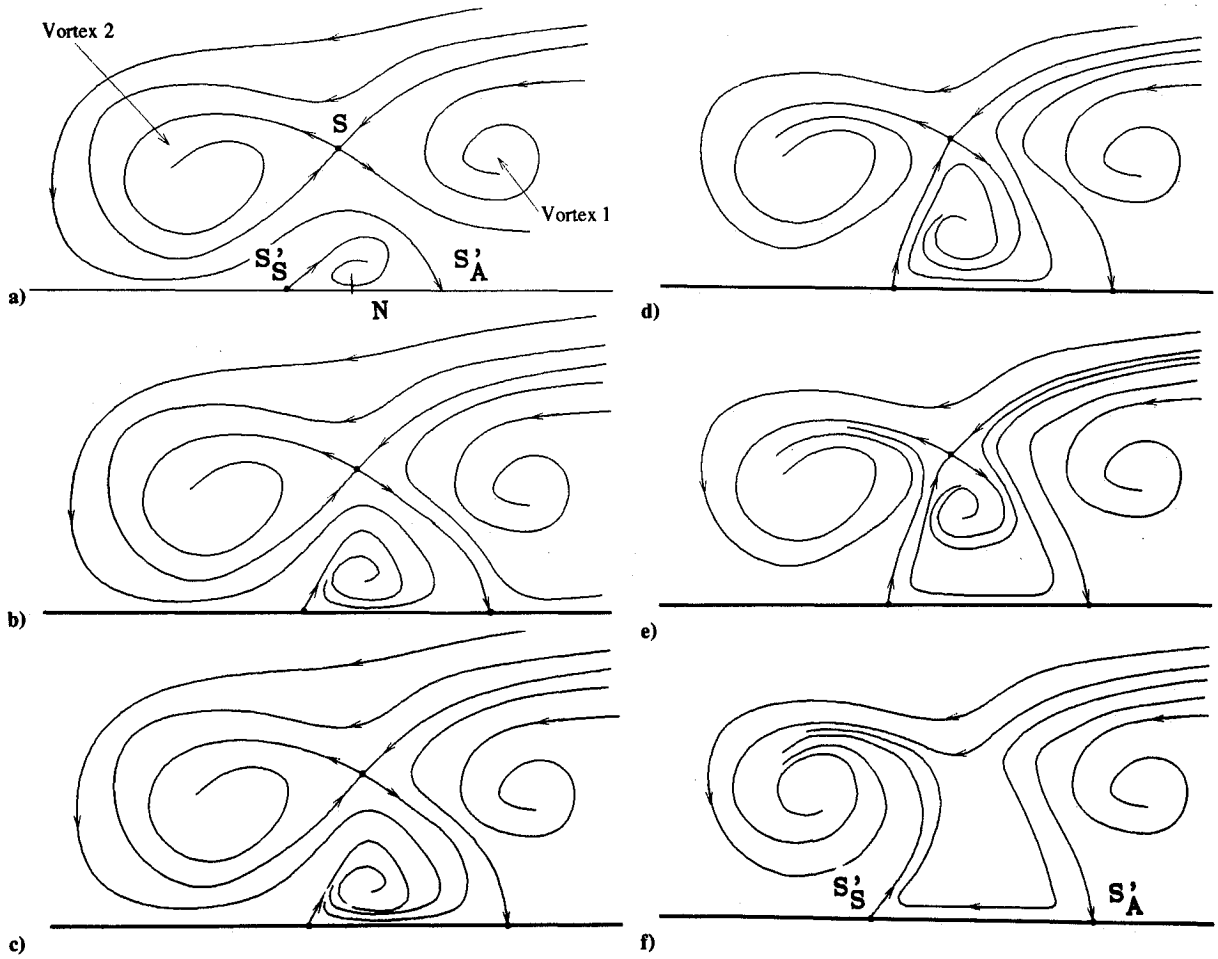

Fig. 14 Unsteady secondary flow topology on symmetry plane.

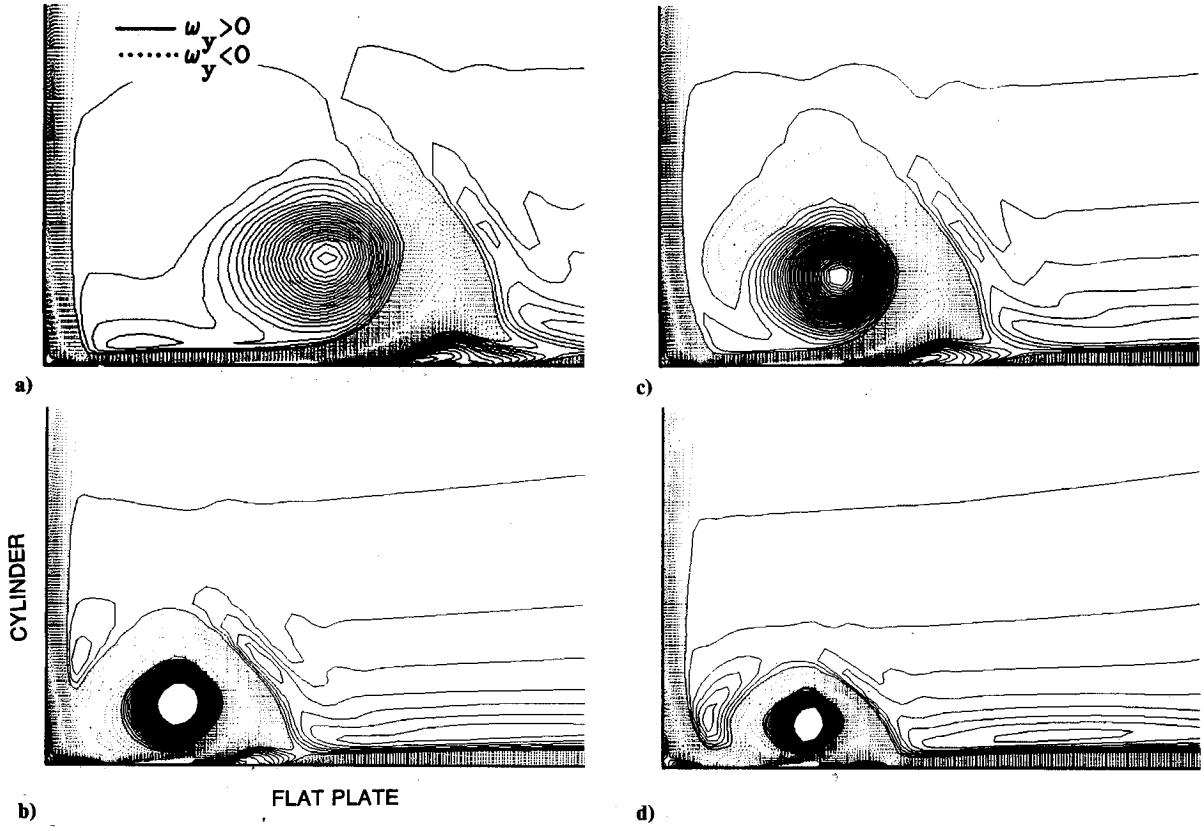

Fig. 15 Isovorticity contours on symmetry plane during horseshoe vortex/surface interaction, $Re_D = 5.4 \times 10^3$ (see Fig. 16a for corresponding time during the cycle).

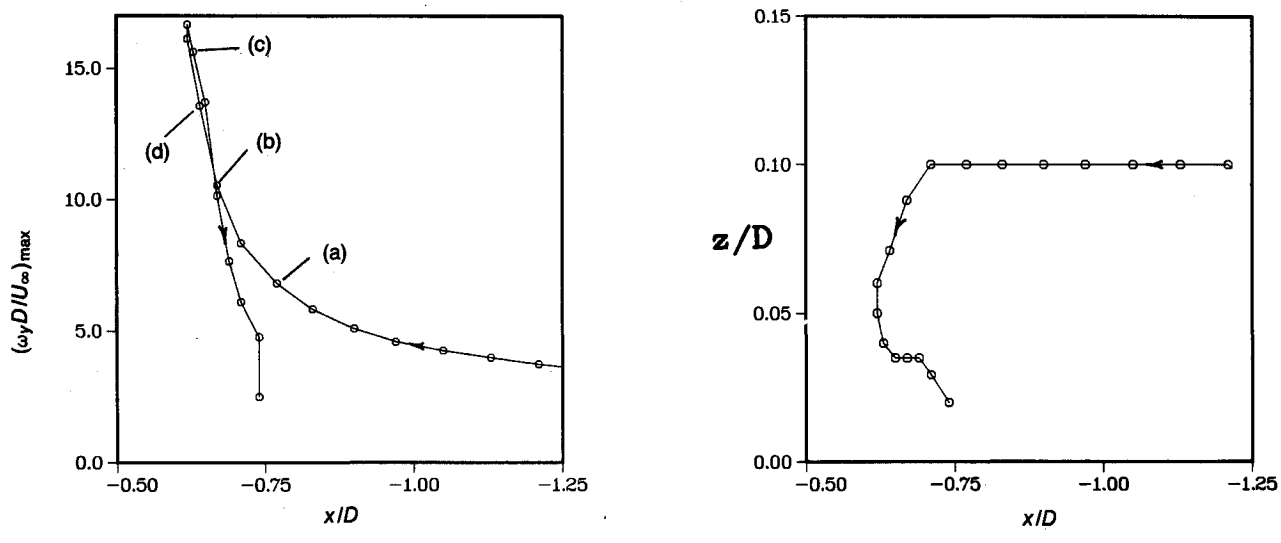

a) Maximum vorticity value in horseshoe vortex core

b) Horseshoe vortex trajectory on symmetry plane

Fig. 16 Strength and trajectory of horseshoe vortex on symmetry plane, $Re_D = 5.4 \times 10^3$.

plane is shown, this vortex/surface interaction was observed at all azimuthal stations in front of the juncture.

3) Subsequently, the horseshoe vortex begins to move upstream away from the cylinder and downward toward the plate (Fig. 16b). At this stage, the secondary flow topology evolves from that of Fig. 14f to the pattern of Fig. 14a. As Fig. 16a indicates, the magnitude of vorticity decreases drastically due to viscous dissipation, which is set up by the large vorticity gradients generated during the vortex stretching process. This is further enhanced by the sheath of opposite vorticity surrounding the horseshoe vortex and by the motion of the vortex toward the plate. The vortex seems to fully dissipate just as a new horseshoe vortex reaches the juncture. The dissipation of the horseshoe vortex, which occurs before another vortex arrives, is an essential mechanism in the cyclic process. If the horseshoe vortex would not dissipate but instead combine with the new incoming vortex, vorticity would continually accumulate in front of the cylinder, a process that would be incompatible with the observed periodicity of the flow.

The computed unsteady horseshoe vortex phenomena upstream of the juncture is in overall agreement with the experimental flow visualizations of Thomas.[7] The details of the

flow topologies on the symmetry plane are, however, different. The streamline patterns inferred by Thomas[7] display the standard topology corresponding to $\beta_P > 1$. Unfortunately, it is not clear from Ref. 7 how much of the reported topology was simply conjectured due to insufficient resolution in the flow visualizations.

In regard to the two different types of flow topology and the horseshoe vortex system unsteadiness, an interesting observation can be drawn from the present computational study. The computed horseshoe vortex array of Fig. 11 for which $Re_D = 5 \times 10^3$ and $\beta_P > 1$ was found to be steady. On the other hand, for the new flow topology ($\beta_P < 1$), the computed vortex system was already unstable at $Re_D = 4 \times 10^3$. The effect of the separation parameter β_P on the onset and type of horseshoe vortex unsteadiness deserves further investigation.

Additional periodic horseshoe vortex computations and comparison with detailed experimental measurements (not presently available) are required. Enhanced numerical resolution behind the juncture is also needed in order to describe the experimentally observed[7] vortex pinchoff mechanism and its correlation with the previously discussed flow events upstream of the cylinder. Enhanced grid resolution near the node of attachment (Fig. 13d) could also result in more primary horseshoe vortices being formed. This, however, is not expected to alter the basic unsteady process already found.

Finally, two additional points can be made regarding the present unsteady results. First, the computational approach, despite its inherent limitations, is capable of reproducing the experimentally observed transition from steady to periodic laminar horseshoe vortex flow. Second, the computed results, obtained on a symmetric juncture configuration, confirm that the unsteady process is produced by a natural instability of the horseshoe vortex array rather than by Karman-vortex shedding in the wake of the cylinder.

IV. Conclusions

A numerical study was performed for both steady and periodic laminar horseshoe vortex systems formed upstream of a cylinder/flat plate juncture. The flowfields were simulated using the full three-dimensional unsteady Navier-Stokes equations and a time-accurate implicit algorithm. The main conclusions are the following.

1) A new type of laminar horseshoe vortex topology, not previously recognized in the literature, has emerged from the present study. Portions of this new topology were analytically shown to be possible by Perry and Fairlie.[11] Furthermore, recent experimental flow visualizations (which became available after the present computations) confirm the predicted new topology. The type of flow topology that exists upstream of the juncture is governed by a separation parameter β_P whose dependence on the flow parameters Re_D, δ_o, and h/D remains to be studied. For $\beta_P > 1$, the standard horseshoe vortex topology is obtained, whereas for $\beta_P < 1$, the new pattern emerges. The skin-friction portrait on the plate is identical for both topologies. However, for the new topology, the outermost line of coalescense is an attachment line and not a separation line. This unusual feature illustrates the fact that convergence of skin-friction lines is a necessary but not sufficient condition for separation.

2) As the Reynolds number increases, the computed flow topology evolves from a single to multiple primary horseshoe vortices, in accordance with experimental observations. At least two different types of triple primary horseshoe vortex systems are shown to be possible. For $\beta_P > 1$, the computed horseshoe vortex array displayed the standard jet-maze topology described in the literature. The predicted new multiple vortex topology obtained for $\beta_P < 1$ requires experimental verification.

3) For $Re_D = 4 \times 10^3$ and 5.4×10^3 (with $\beta_P < 1$), the computed juncture flow becomes unsteady and cyclic, with a frequency that increases with Reynolds number. The unsteady process is characterized by 1) the periodic generation of horseshoe vortices downstream of the point of attachment, 2) the convection of the vortices toward the juncture, 3) vorticity intensification by vortex stretching, 4) a dramatic vortex/surface interaction that displays the eruption of vorticity from the plate boundary layer, and 5) the upstream movement and dissipation of the horseshoe vortex that takes place as a new vortex arrives at the juncture. This computed unsteady horseshoe vortex process upstream of the cylinder is in qualitative agreement with experimental flow visualizations. The computed results, obtained for a symmetric configuration, confirm that the unsteady process is not originated by Karman-vortex shedding in the wake of the cylinder. The present investigation constitutes the first computational study of the periodic laminar horseshoe vortex phenomenon.

Acknowledgments

Computational resources for the present study were provided by NASA Ames Research Center, under the NAS program, and by the Air Force Supercomputer Center, Kirtland AFB, NM. The author is grateful to J. Shang and M. Aftosmis of the Computational Aerodynamics Group for several helpful discussions.

References

[1]Baker, C. J., "The Laminar Horseshoe Vortex," *Journal of Fluid Mechanics*, Vol. 95, Pt. 2, 1979, pp. 347–367.

[2]Eckerle, W. A., and Langston, L. S., "Horseshoe Vortex Formation Around a Cylinder," *Journal of Turbomachinery*, April 1987, pp. 278–285.

[3]Pierce, F. J., and Harsh, M. D., "The Mean Flow Structure Around and Within a Turbulent Junction or Horseshoe Vortex—Part II: The Separated and Junction Vortex Flow," *Journal of Fluids Engineering*, Vol. 110, Dec. 1988, pp. 415–423.

[4]Krothapalli, A., Lourenco, L., and Buchlin, J., "On the Separated Flow Upstream of a Jet in a Cross Flow," AIAA Paper 89-0571, Jan. 1989.

[5]Kitchens, C. W., Jr., Gerber, N., Sedney, R., and Bartos, J. M., "Streamline Vorticity Decay Downstream of a Three-Dimensional Protuberance," ARBRL-TR-02375, Aberdeen Proving Ground, MD, Oct. 1981.

[6]Tobak, M., and Peake, D. J., "Topology of Two-Dimensional and Three-Dimensional Separated Flows," AIAA Paper 79-1480, July 1979.

[7]Thomas, A. S. W., "The Unsteady Characteristics of Laminar Juncture Flow," *Physics of Fluids*, Vol. 30, No. 2, 1987, pp. 283–285.

[8]Kubendran, L. R., Bar-Sever, A., and Harvey, W. D., "Flow Control in a Wing/Fuselage-Type Juncture," AIAA Paper 88-0614, Jan. 1988.

[9]Norman, R. S., "On Obstacle Generated Secondary Flows in Laminar Boundary Layers and Transition to Turbulence," Ph.D. Dissertation, Illinois Inst. Tech., Chicago, IL, Dec. 1972.

[10]Sedney, R., and Kitchens, C. W., Jr., "The Structure of Three-Dimensional Separated Flows in Obstacle-Boundary Layer Interactions," AGARD CP-168, May 1975.

[11]Perry, A. E., and Fairlie, B. W., "Critical Points in Flow Patterns," *Advances in Geophysics*, Vol. 18B, 1974, pp. 299–315.

[12]Beam, R. M., and Warming, R. F., "An Implicit Factored Scheme for the Compressible Navier-Stokes Equations," *AIAA Journal*, Vol. 16, No. 4, 1978, pp. 393–402.

[13]Briley, W. R., Buggelin, R. C., and McDonald, H., "Solution of the Three-Dimensional Navier-Stokes Equations for a Steady Laminar Horseshoe Vortex Flow," AIAA Paper 85-1520, July 1985.

[14]Kaul, U. K., Kwak, D., and Wagner, C., "A Computational Study of Saddle Point Separation and Horseshoe Vortex System," AIAA Paper 85-0182, Jan. 1985.

[15]Pulliam, T. H., and Steger, J. L., "Implicit Finite-Difference Simulation of Three-Dimensional Compressible Flow," *AIAA Journal*, Vol. 18, No. 2, 1980, pp. 159–167.

[16]Schlichting, H., *Boundary Layer Theory*, 6th ed., McGraw-Hill, New York, 1968.

[17] Steger, J., and Chaussee, D., "Generation of Body-Fitted Coordinates Using Hyperbolic Partial Differential Equations," *SIAM Journal of Scientific Statistical Computing*, Vol. 1, Dec. 1980, pp. 431–437.

[18]Visbal, M. R., "Numerical Investigation of Laminar Juncture Flows," AIAA Paper 89-1873, June 1989.

[19]Webster, W. P., and Shang, J. S., "Comparison Between Thin-Layer and Full Navier-Stokes Simulations Over a Supersonic Delta Wing," AIAA Paper 90-0589, Jan. 1990.

[20]Gordnier, R. E., and Visbal, M. R., "Unsteady Navier-Stokes Solutions for a Low Aspect Ratio Delta Wing," AIAA Paper 90-1538, June 1990.

[21]Kawahashi, M., and Hosoi, K., "Beam-Sweep Laser Speckle Velocimetry," *Experiments in Fluids*, Vol. 8, No. 1/2, 1989, pp. 109–111.

[22]Dallmann, U. "Topological Structures of Three-Dimensional Vortex Flow Separation," AIAA Paper 83-1735, July 1983.

[23]Chapman, G. T., "Topological Classification of Flow Separation on Three-Dimensional Bodies," AIAA Paper 86-0485, Jan. 1986.

[24]Tobak, M., and Peake, D. J., "Topology of Three-Dimensional Separated Flows," *Annual Review of Fluid Mechanics*, Vol. 14, 1982, pp. 61–85.

[25]Hunt, J. C. R., Abell, C. J., Peterka, J. A., and Woo, H., "Kinematical Studies of the Flows Around Free or Surface-Mounted Obstacles; Applying Topology to Flow Visualization," *Journal of Fluid Mechanics*, Vol. 86, Pt. 1, 1978, pp. 179–200.

[26]Perry, A. E., and Chong, M. S., "A Series-Expansion Study of the Navier-Stokes Equations with Applications to Three-Dimensional Separation Patterns," *Journal of Fluid Mechanics*, Vol. 173, Dec. 1986, pp. 207–223.